Title

Lattice oxygen-mediated NiOOM formation for efficient oxygen evolution reaction in MOF@LDH core—shell structures

Authors

Liu, Ziqi

Li, Haoyu

Kang, Hung-Sen

et al.

Publication Date

2023-02-01

DOI

10.1016/j.cej.2022.140403

Chemical Engineering Journal 454 (2023) 140403

Contents lists available at ScienceDirect

Chemical Engineering Journal

journal homepage: www.elsevier.com/locate/cej

Lattice oxygen-mediated Ni—O—O—M formation for efficient oxygen evolution reaction in MOF@LDH core–shell structures

Ziqi Liu [a], Haoyu Li [a], Hung-Sen Kang [a], Alpha T. N'Diaye [b], Min Hwan Lee [a,*]

[a] Department of Mechanical Engineering, University of California, Merced, CA 95343, United States
[b] Lawrence Berkeley National Laboratory, Berkeley, 94720 CA, United States

ARTICLE INFO

Keywords:
Oxygen evolution reaction
Layered double hydroxide
Metal–organic framework
Core–shell structure
Lattice oxygen-mediated mechanism

ABSTRACT

Two-dimensional (2D) layered double hydroxides (LDHs) are promising as an effective electrocatalyst towards oxygen evolution reaction (OER), but their poor conductivity and tendency to stack together limits their activity and durability as an electrocatalyst. Herein, a three-dimensional (3D) core–shell catalyst, in which numerous LDH nanoplates are vertically grown on cuboidal metal organic framework (MOF) structures, is synthesized through a facile one-pot reaction strategy. The representative electrocatalyst (CoNi-BDC@LDH) achieves an excellent OER performance (with an overpotential of 282 mV at 100 mA cm^{-2}) and stability. A series of *quasi-operando* and *ex-situ* characterization reveals a lattice oxygen-mediated mechanism where Ni and its neighboring metal site collaboratively forms Ni-O-O-M (M = Ni, Co) bridges, and the high valence state of Ni facilitates O_2 desorption from the bridges. The high OER performance is additionally attributed to γ-NiOOH and CoOOH phases, and a large electrochemically active surface area.

1. Introduction

With ever increasing energy consumption and carbon emissions, there is an impending demand for highly efficient and economical renewable energy systems [1]. Hydrogen is considered a promising clean energy medium to address the unpredictable intermittency of renewable energy with a high heat value [2]. Electrochemical water splitting is the most promising clean approach to generate high purity of hydrogen. Between two half reactions of water splitting – hydrogen evolution reaction (HER) and oxygen evolution reaction (OER) [3] – OER is the main rate-limiting half-reaction due to its slow four-electron transfer process and high activation barrier [4,5]. While IrO_2 and RuO_2 have been accepted as the standard OER catalysts because of their high catalytic activity [6–8], their prohibitive cost, rarity, and limited durability preclude their widespread use [9].

Recently, transition metal-based 2D layered double hydroxides (LDHs) have attracted great attention for OER catalysis due to their remarkable tunability of structural composition, physicochemical properties, and facile synthesis process [10–13]. This material class can be represented by a general formula as $[M^{II}_{1-x}M^{III}_x(OH)_2]_{z+}(A^{n-})_{z/n}{\cdot}yH_2O$, where M^{II} and M^{III} are metallic divalent and trivalent cations, and A^{n-} represents the interlayer anions. The flexible choices of M^{II}, M^{III} and A^{n-} and the variability of interlayer distances in the LDH structure allow further improvement of OER performance [14]. However, the LDH family exhibits a low electrical conductivity [15,16], significantly limiting their electrocatalytic performance. Moreover, the structure may collapse and undergo a severe aggregation of active species due to the micropores and defects formed during the synthesis process [17,18]. Therefore, developing a synthetic approach that can leverage the benefits of LDHs while avoiding the structural degradation is essential for enabling efficient and durable electrocatalysis.

Three-dimensional (3D) carbon structures are considered as a promising framework for the growth of LDHs to maximize the surface area for reactant access and provide efficient charge transport through the resultant hybrid catalysts. In addition, the 3D structures are expected to deter the aggregation of LDHs while providing more of catalytically active edge sites. Much efforts have been devoted to design 3D LDH configurations for efficient OER activity, but most of them require a tedious and costly synthesis process, limiting their commercial viability [19–24].

In this study, we present a simple one-pot strategy for the preparation of high-performance 3D core–shell LDH electrocatalysts derived from a metal–organic framework (MOF). A hierarchical CoNi-BDC@LDH electrocatalyst with a highly dispersed 3D core (MOF) -

* Corresponding author.
E-mail address: mlee49@ucmerced.edu (M.H. Lee).

https://doi.org/10.1016/j.cej.2022.140403
Received 24 August 2022; Received in revised form 4 November 2022; Accepted 13 November 2022
Available online 17 November 2022

shell (LDH) structure is prepared via a one-step hydrothermal step using Ni foam as the substrate. For the process, terephthalic acid is employed as the organic ligand for the MOF precursor, and urea as the surface coordination buffer between LDHs and MOF. The dissolution of the inner "core" and the precipitation of cations caused by the release of hydroxide from urea during the hydrothermal process result in the formation of a "shell" made of numerous LDH nanoplates on the outer layer of MOF structure [25]. The resultant 3D cuboidal structure with numerous nanoplate cloths exhibits a low overpotential of 282 mV at 100 mA cm^{-2} and excellent cyclic and chronoamperometric stability for OER. A series of *quasi-operando* characterization by Raman, Fourier transform infrared spectroscopy (FTIR) and X-ray phostoelectron spectroscopy (XPS) along with *ex situ* X-ray absorption spectroscopy (XAS) are further performed to reveal intrinsic active sites and provide a mechanistic interpretation of OER process in the 3D catalyst. The main active sites are believed to reside at bimetallic Ni-Co sites at the interface between the MOF and LDH structures, rather than within MOF or LDH themselves, suggesting a promising route of synthesizing high-performance OER catalysts.

2. Experimental section

2.1. Materials and chemicals

Cobalt nitrate hexahydrate ($Co(NO_3)_2{\cdot}6H_2O$, 99.8 %), nickel nitrate hexahydrate ($Ni(NO_3)_2{\cdot}6H_2O$, 99.8 %), urea (NH_2CONH_2, 98.0 %), N,N-Dimethylformamide (DMF, 99.8 %) and potassium hydroxide (KOH) were purchased from Sigma-Aldrich. Ethanol (C_2H_5OH, 99.5 %), IrO_2 (99.9 %) and terephthalic acid (BDC; $C_8H_6O_4$, > 98 %) were supplied by Alfa Aesar. All chemicals were used as received without further purification. A nickel foam (3 × 2.5 cm^2) was soaked into 2 M HCl in an ultrasonic cleaner for 15 min. Then it was washed with deionized water and ethanol for 10 min and dried under N_2 flow.

2.2. Synthesis of CoNi-BDC@LDH and CoNi-LDH

Both CoNi-BDC@LDH and CoNi-LDH were prepared via a one-pot hydrothermal reaction. First, a precursor solution was prepared for each hydrothermal reaction. For CoNi-BDC@LDH, terephthalic acid (166 mg) and urea (300 mg) were dissolved and sonicated in a mixture of 20 mL DMF and 20 mL deionized water. Then, $Co(NO_3)_2{\cdot}6H_2O$ (290 mg) and $Ni(NO_3)_2{\cdot}6H_2O$ (290 mg) were added in the solution and sonicated for 30 min. For CoNi-LDH, urea (300 mg), $Co(NO_3)_2{\cdot}6H_2O$ (290 mg), and $Ni(NO_3)_2{\cdot}6H_2O$ (290 mg) were dissolved and sonicated in a mixture of 40 mL deionized water and sonicated for 30 min. The prepared solution was then transferred into a 40 mL Teflon-lined stainless-steel autoclave together with an as-cleaned nickel foam (3 × 2.5 cm^2) and heated in an oven at 120 °C for 12 h. After cooling down to room temperature, the resultant sample was washed with deionized water and ethanol with ultrasonic cleaner for 15 min and dried at 80 °C for 12 h in air to obtain CoNi-BDC@LDH or CoNi-LDH.

2.3. Synthesis of Co-BDC@LDH and Ni-BDC@LDH

Both Co-BDC@LDH and Ni-BDC@LDH were prepared by a two-step hydrothermal reaction. For Co-BDC@LDH, 290 mg of $Co(NO_3)_2{\cdot}6H_2O$ was first dissolved into 20 mL deionized water, and 155 mg of terephthalic acid was separately dissolved into 20 mL DMF. The two solutions were mixed and ultrasonicated for 30 min at room temperature. The mixed solution together with a cleaned Ni foam (3 × 2.5 cm^2) was transferred into a Taflon-lined stainless-steel autoclave and heated in an oven at 120 °C for 12 h. The resultant samples were collected and rinsed with water for 30 min to obtain Co-BDC grown on a nickel foam. Then, 290 mg of $Ni(NO_3)_2{\cdot}6H_2O$, 300 mg of urea was dissolved into 40 mL deionized water where Co-BDC was added into an autoclave and heated at 120 °C for 12 h again. The product was washed with deionized water and ethanol and dried in air at 80 °C for 12 h to obtain Co-BDC@LDH. The synthesis procedure for Ni-BDC@LDH is the same as that of Co-BDC@LDH, except for the order of introducing Co and Ni precursors.

2.4. Physical characterization

The morphology and microstructure were characterized by scanning electron microscopy (SEM; Zeiss Gemini SEM 500, 3 kV) and transmission electron microscopy (TEM; Philips CM300 FEG system 200 kV). X-ray diffraction (XRD) patterns were recorded using PAN analytical X'Pert PRO with Co Kα radiation ($\lambda = 1.78897$ Å) at the step size of 0.02° and scan rate of 0.04° s^{-1}, and the resulting data was converted to Cu Kα radiation (λ = 1.5418 Å) for the analysis. FTIR were recorded on a Nicolet 380 FTIR Spectrometer with the wave numbers from 400 to 4,000 cm^{-1} by dispersing samples onto a crystal attenuated total reflectance (ATR) accessory. XPS was performed on a PHI Quantum 2000 system using a focused, monochromatic Al Kα X-ray (1486.6 eV) source for excitation and a spherical section analyzer (200 μm diameter X-ray beam incident to the surface normal; detector set at 45°). Raman spectra were obtained on an iXR Raman spectrometer (Thermo Scientific). XAS were performed in total electron yield mode at beamline 6.3.1 of the Advanced Light Source (ALS). *Quasi-operando* XRD, XPS, Raman and ATR FTIR were performed on samples that were exposed to a specific potential for 15 min.

2.5. Electrochemical characterization

The OER characterization was performed in a standard three-electrode glass cell by a potentiostat (SP-200, Bio-Logic SAS) at room temperature. The as-prepared samples supported on nickel foam was used as the working electrode while a graphite rod and an Ag/AgCl (1 M KOH) electrode were used as the counter and reference electrodes, respectively. All potentials were expressed with respect to reversible hydrogen electrode (RHE). The overpotential (η) was calculated by η (V) = V (RHE) − 1.23 V. O_2 flow was fed into the 1 M KOH electrolyte for > 30 min. The solution was put on a magnetic stirrer rotating at 500 rpm. All linear sweep voltammetry (LSV) polarization curves were corrected by eliminating iR drop based on the ohmic resistant obtained from EIS measurements. Electrochemical impedance spectroscopy (EIS) measurements were tested on a SP-200 system (Bio-Logic SAS) with an AC bias of 10 mV in the frequency range of 0.1 Hz – 100 kHz. Before all the LSV tests, the electrodes were cycled at 100 mV s^{-1} until reproducible cyclic voltammograms were obtained. Tafel slopes were obtained after an iR correction. The electrochemically active surface areas (ECSA) were characterized by cyclic sweep with various scan rates (2 to 10 mV s^{-1} at an interval of 2 mV s^{-1}) in a small range where no noticeable faradaic reaction occurs (1.13–1.18 V).

3. Results and discussion

3.1. Physicochemical characterization of as-prepared samples

The CoNi-BDC@LDH core–shell microstructures is synthesized directly via a one-step hydrothermal reaction as depicted in Fig. 1. Two additional MOF-derived LDH structures are synthesized via a two-step hydrothermal reaction. One is by growing LDH on Co-BDC MOF (namely, Co-BDC@LDH), and the other is by growing LDH on Ni-BDC MOF (namely, Ni-BDC@LDH). A detailed synthesis procedure is provided in the Experimental.

As shown in the SEM images in Fig. 2a, 2b, and S1, CoNi-BDC@LDH manifests a cuboid shape, unlike the other BDC@LDH variants (Fig. S2). The zoomed-in SEM image in Fig. 2b reveals that nanoplates with a thickness of ~ 10 nm are vertically formed on the surface of MOF substrate, resulting in an overall core–shell structure where each cuboidal MOF is surrounded by numerous LDH nanoplates with needle-like features on the edge of the nanoplates. The fine LDH nanoplates on the BDC

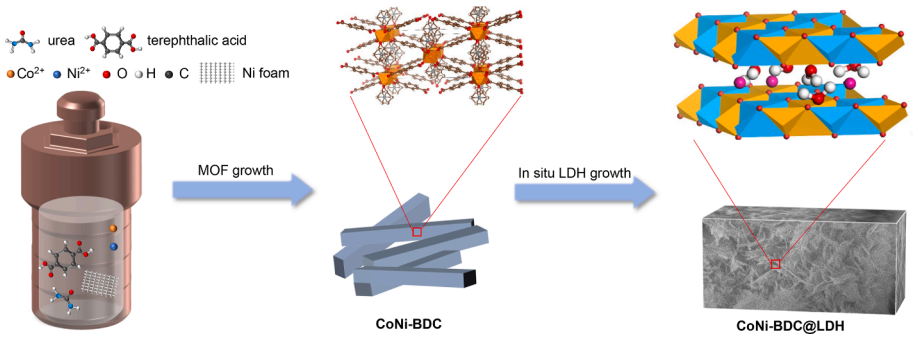

Fig. 1. Schematic illustration of the synthesis process for hierarchical CoNi-BDC@LDH core–shell structure.

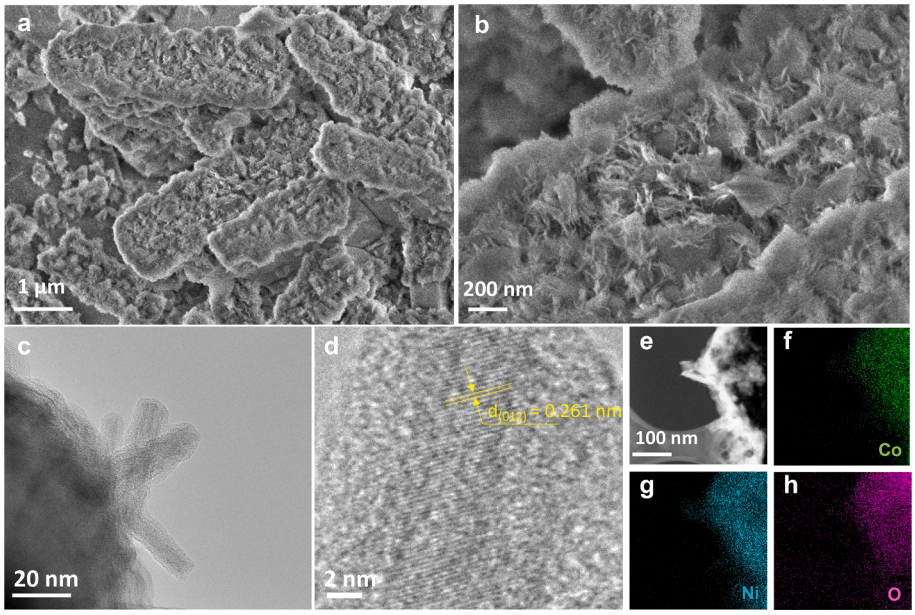

Fig. 2. (a,b) SEM images, (c) a TEM image, (d) a HR-TEM image, (e-h) EDS elemental mappings of CoNi-BDC@LDH.

structure that are clearly visible in CoNi-BDC@LDH are not distinct in the other two BDC@LDH structures (Fig. S2). The TEM images in Fig. 2c and S3 reassures the formation of a core–shell structure in CoNi-BDC@LDH. The high-resolution TEM (HRTEM) image in Fig. 2d displays clear lattice fringes with an interplanar distance of 0.261 nm, corresponding to (012) planes of CoNi-LDH [26]. The same lattice fringes are also found in Ni-BDC@LDH and Co-BDC@LDH as shown in Fig. S4, supporting the formation of LDH structures in these samples. Energy-dispersive X-ray spectroscopy (EDS) elemental maps in Fig. 2e–2 h indicate that Co, Ni, and O species are uniformly dispersed throughout the structure.

The structural information of as-prepared samples is obtained by XRD (Fig. S6a). The peaks located at 40.2° and 46.8° are found in all samples and ascribed to the bimetallic Co and Ni-based LDH structure, which is supported by the corresponding peaks from CoNi-LDH sample. Since the nanoplate-like LDH structures are not explicitly visible in Co-BDC@LDH and Ni-BDC@LDH despite the distinct diffraction peaks and TEM lattice fringes corresponding to LDH, we conjecture a considerable fraction of the LDHs in these two samples are formed inside the BDC structure rather than onto the structure. CoNi-BDC@LDH shows additional distinct peaks unlike the other samples. The peaks located at 23.7° and 35.1° are assigned to the characteristic peaks of (006) and (012) planes of α-$Ni(OH)_2$, representing the typical hydrotalcite-type structure of LDH (JCPDS# 38–0715) while the peaks located at 18.9°, 33.4° and 38.9° correspond to (001), (100) and (101) planes of β-$Ni(OH)_2$ (JCPDS# 14–0117) [27]. CoNi-BDC@LDH exhibits additional peaks at 18.4°, 32.2° and 50.9°, which can be indexed to the (001), (100), and (102) planes of CoOOH (JCPDS# 30–0443) [28]. In the FTIR spectra (Fig. S6b), all the BDC@LDH samples show the isocyanate (N═C═O) stretching mode (~2,283 cm^{-1}). Given the absence of isocyanate peak in CoNi-LDH (from Fig. S6b) and BDC structure (from the ref. [29]), the appearance of the isocyanate peak in BDC@LDH samples are ascribed to the urea-aided chemical bonding between the BDC structure and LDH. The MOF structure resulting from trivalent metal centers and terephthalic acid(benzene-1,4-dicarboxylate) linker molecules, which is named as MIL-53, consists of M−OH chains that are bonded to 4 neighboring chains [30,31]. The peaks at ~ 617 cm^{-1} and ~ 570 cm^{-1} corresponding to Ni-OH and Co-OH bending vibrations visible on all three BDC@LDH variants also support the formation of CoNi-based MIL-53 MOF in these samples.

In the Raman spectra (Fig. S7), all three BDC@LDH samples exhibit certain I_D and I_G band located at ~ 1,418 cm^{-1} and 1,618 cm^{-1}, respectively, indicating their formation of a carbon network. Significant blue shifts of D and G bands from the standard I_D and I_G locations (~1,340 cm^{-1} and 1,510 cm^{-1}) can be related to the strain effect caused by the interaction between BDC and LDH surfaces [32]. The I_D/I_G ratio is calculated to be 1.01, 0.9 and 0.95 for CoNi-BDC@LDH, Ni-BDC@LDH and Co-BDC@LDH, respectively. Their similarity in the I_D/I_G ratios suggests they have a similar level of defect concentrations. On the other hand, no obvious I_D and I_G bands are detected for CoNi-LDH (Fig. S7a),

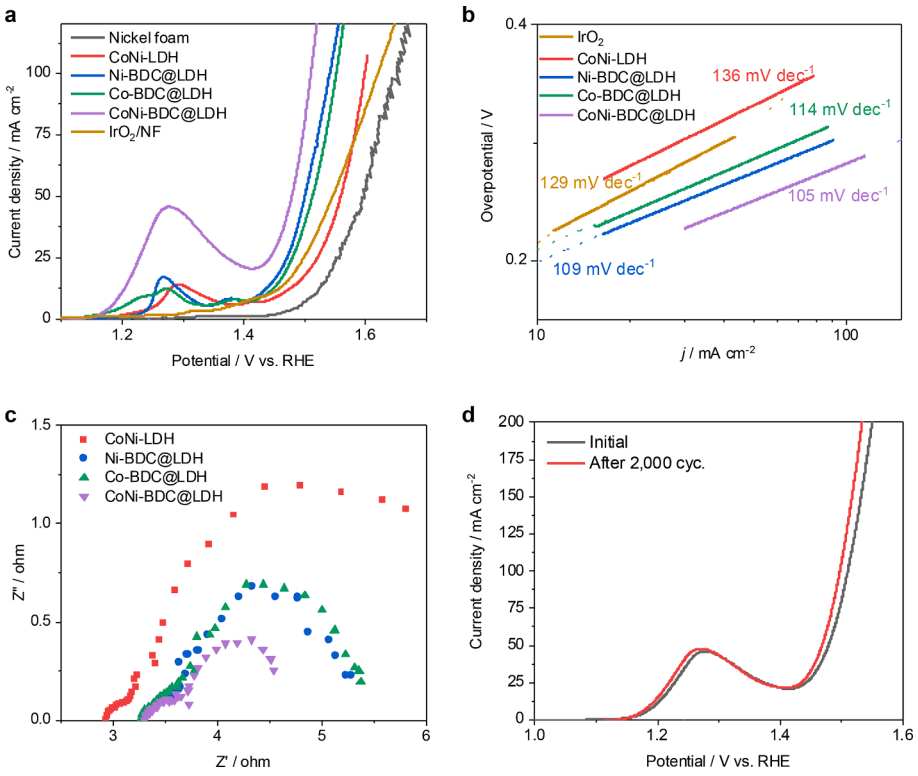

Fig. 3. (a) OER polarization curves after iR-compensation. (b) OER Tafel slopes of CoNi-LDH, Ni-BDC@LDH, Co-BDC@LDH, CoNi-BDC@LDH, and IrO_2 benchmark. The horizontal axis is in a logarithmic scale. (c) Nyquist plots (at the potential of 1.53 V vs RHE) of as-prepared catalysts, (d) OER polarization curves for CoNi-BDC@LDH before and after 2,000 cycles between 1.0 V and 1.8 V at 5 mV s^{-1}.

consistent with the fact that carbon element mostly exists in the form of CO_3^{2-} within the interlayers of LDH structure [10]. Low-frequency Raman spectra are additionally obtained (Fig. S7b) to identify metal oxygen (M−O) vibrations. The peaks at 319, 455 and 526 cm^{-1} are attributed to the M−O vibrations of $Co(OH)_2$ and $Ni(OH)_2$, in accordance with the previously reported Ni-Co systems [33,34]. The 550 cm^{-1} peak is attributed to NiOOH [35], and those at 739 and 812 cm^{-1} correspond to the stretching mode of benzene ring from BDC substrate [29,36].

3.2. Electrochemical characterization

The electrochemical OER performance is examined in 1 M KOH in a standard three-electrode setup. As shown in the LSV curve shown in Fig. 3a, CoNi-BDC@LDH exhibits the best OER performance; it reaches 100 mA cm^{-2} at a potential as low as 1.512 V vs RHE at 5 mV s^{-1}, which corresponds to an overpotential of 282 mV. The benchmark IrO_2 necessitates an overpotential of 390 mV for the same current density (Fig. S8). All the BDC@LDH variants exhibit an enhanced performance compared to the bare LDH sample (i.e., CoNi-LDH). The peaks appearing at ~ 1.25 – 1.3 V in the polarization curves are mainly ascribed to the oxidation peak of Ni^{2+} [37–39]. In the backswept LSV provided in Fig. S9, the Ni^{2+} oxidation peak is absent revealing the OER curve more explicitly. The OER kinetics is also assessed by the Tafel plots in Fig. 3b. CoNi-BDC@LDH possesses the lowest Tafel slope of 105 mV dec^{-1}, which is smaller than those of CoNi-LDH (136 mV dec^{-1}), Co-BDC@LDH (115 mV dec^{-1}) and Ni-BDC@LDH (109 mV dec^{-1}), reflecting its faster charge transfer. An important indicator of intrinsic activity of a catalyst is turnover frequency (TOF); a greater TOF signifies a better atom consumption efficiency and faster kinetics per active site. Assuming Co and Ni atoms are all active during the OER process, TOFs are calculated for all samples at an overpotential of 300 mV. As shown in Fig. S10, CoNi-BDC@LDH shows the highest TOF (0.09 s^{-1}) among all samples, reflecting that the sample has a faster kinetics toward OER. According to the EIS performed at 1.53 V vs RHE (Fig. 3c), CoNi-BDC@LDH shows the smallest arc size, again indicating a more efficient charge transfer during OER. It is noted that the smaller arc at a higher frequency range is likely originated from electrolyte conduction since the arc size is negligent of the potential applied during the measurement. The OER LSV curves of CoNi-BDC@LDH before and after 2,000 CV cycles (Fig. 3d) indicates that the overpotential becomes even slightly smaller after 2,000 cycles. While the morphology of the sample remains virtually unchanged after 2,000 cycles (Fig. S12), the samples show a change in surface chemistry as confirmed by XPS (Fig. S13). The slightly enhanced OER performance after 2,000 cycles is partially ascribed to the increase of oxygen defects, as indicated by the O 1 s peak at ~ 531 eV. In a chronoamperometric testing (Fig. S14), CoNi-BDC@LDH maintains its current density at ~ 22 mA cm^{-2} after 20 h, further revealing the superior stability.

The ECSA is calculated by the double-layer capacitance (C_{dl}) to support the improved OER catalytic activity of as-prepared samples. As demonstrated in Figs. S15 and S16, C_{dl} of CoNi-BDC@LDH is determined to be 169.9 μF cm^{-2}, which is significantly higher than those of CoNi-LDH (20.9 μF cm^{-2}), Co-BDC@LDH (20.2 μF cm^{-2}) and Ni-BDC@LDH (26.9 μF cm^{-2}). The quantified ECSA of CoNi-BDC@LDH is 1.062 cm^2 (Table S1); its high ESCA indicates that it possesses a large exposed active area than the other catalysts, further making it favorable for OER.

We performed additional SEM, TEM and XRD on CoNi-BDC@LDH after a one-time potential sweep from 1.2 V to 1.8 V versus RHE at 5 mV s^{-1} (Fig. S11). While the post-OER sample seen by TEM is similar to that of the as-prepared sample, its morphology as seen by SEM seems to have lost some of the fine needle-like features on the edge of LDHs. However, all the notable XRD peaks from the as-prepared sample are also found in the post-OER sample.

3.3. Differences in surface chemistry among catalysts

XPS analysis is performed to explore surface chemistry and reveal the electrocatalytically active sites. The greatly decreased C═O peak intensity in C 1 s peak for CoNi-BDC@LDH compared to other samples (Fig. S19a) suggests that C═O probably acted as a nucleation center for the growth of LDH on the surface of BDCs. It is noted that the ratio of O_β (corresponding to oxygen defects) in CoNi-BDC@LDH is 41.5 %, higher than those of CoNi-LDH (27.8 %), Ni-BDC@LDH (36.8 %), and Co-BDC@LDH (33.3 %) as shown in Fig. S19b. This is aligned with the OER performance described above because oxygen vacancy is widely known to act as an active site for OER. Little difference is observed in the nickel valence states among the samples (Fig. S20a). The broader width of Ni^{3+} peak for CoNi-BDC@LDH suggests the existence of γ-NiOOH, which is believed to be beneficial to the OER performance [40]. CoNi-BDC@LDH has a Co^{3+}/Co^{2+} ratio of 0.87 (Fig. S20b), significantly larger than CoNi-LDH (0.37). This is aligned with the XRD analysis showing the formation of CoOOH in CoNi-BDC@LDH, which is additionally beneficial to the OER kinetics [16].

To further study the effect of interatomic bonding and cationic valence states on OER activity, XAS is additionally performed. Fig. 4a shows the polarization-dependent C K-edge spectra of as-prepared samples. The spectra exhibit a strong transition mode of C 1 s → π^* at ~ 285.5 eV and a broad 1 s → σ^* at ~ 292.0 eV [42]. In the O K-edge spectra presented in Fig. 4b, the features between ~ 529 eV and 535 eV reflect the structure of the empty electronic states from O 1 s electronic level to O 2p orbitals that is hybridized strongly with the transition metal 3d orbitals [43]. The peak at ~ 530.6 eV (Co 3d/O 2p) for CoNi-BDC@LDH is stronger and exhibits a positive shift by ~ 0.2 eV compared to that of CoNi-LDH, indicating Co species are partially oxidized in CoNi-BDC@LDH. Meanwhile, a distinct drop in the peak intensity at 532.8 eV and a negative shift by ~ 0.2 eV in CoNi-BDC@LDH is attributed to the formation of oxygen vacancies and the weakening of Ni 3d and O 2p hybridization [44,45]. This will facilitate the adsorption of OH^- to the active site (i.e., oxygen vacancies next to Ni sites), thus increasing the interactions between surface metal ions and adsorbed oxygen intermediates.

The L-edge spectra (Fig. 4c and 4d) are useful for the analysis of transition metal d orbitals, as the 2p → 3d L-edge transition is a dipole-allowed excitation [46]. As a result of 2p spin-orbital coupling interaction, the Co L-edge (Fig. 4c) split into two regions: one in a lower energy L3-edge ($2p_{3/2}$ → 3d) at ~ 778 eV and the other in a higher energy L2-edge ($2p_{1/2}$ → 3d) at ~ 793 eV. The L3 edge peak is further split into a mixture of tetrahedrally coordinated Co^{2+} and octahedrally coordinated Co^{3+} [47]. CoNi-BDC@LDH shows a markedly intensified peak in the high energy region (779.6 eV), suggesting an increase of Co^{3+}/Co^{2+} ratio. Furthermore, the Ni L-edge X-ray absorption (Fig. 4d) also indicates that BDC-based samples have a higher Ni valance state than that of CoNi-LDH, which does not exhibit a distinct Ni^{3+} peak at ~ 834 eV unlike the other samples. The XAS spectra are consistent with the electrochemical results that CoNi-BDC@LDH possesses a higher OER activity, which are mainly attributed to a larger amount of oxygen vacancies and higher valence states of Co and Ni [48].

3.4. Quasi-operando analysis on CoNi-BDC@LDH

To further reveal the catalytically active sites of CoNi-BDC@LDH, the changes in local atomic environment and valence states are observed via a *quasi-operando* characterization scheme. Since the usual characterization process prohibits a true *in situ* study due to their instrumental limitations (such as the need for a high vacuum environment), we performed a series of *ex situ* characterization by Raman spectroscopy, FTIR, XPS, and XAS after exposing the samples to a specific electrochemical environment for a set duration, mimicking the scenario where a true *in situ* measurement would result in. CoNi-BDC@LDH is exposed to different potentials (1.33 V, 1.43 V, 1.53 V and 1.63 V) for 15 min in 1 M KOH before an *ex-situ* characterization. Raman spectra are obtained at different overpotentials (Fig. S22). At a potential of 1.43 V or less, there are only two distinct peaks at 455 and 526 cm^{-1}, which correspond to Ni $(OH)_2$. At a higher potential, however, signals from slightly higher Raman shift values (~479 and 557 cm^{-1}) start to emerge, which is ascribed to the formation of γ-NiOOH [35,49,50]. The emergence of NiOOH is further supported by a post-OER O K-edge XAS spectra shown in Fig. S21 (at ~ 528 eV). The transformation of $Ni(OH)_2$ into γ-NiOOH, hence the effective oxidation of Ni (from Ni^{2+} to Ni^{3+}) during OER process further confirms the active role of Ni cations in OER.

Attenuated total reflection (ATR) FTIR provides information of the functional groups near the surface, which allows to detect surface alterations during OER. A zoomed-in ATR-FTIR in Fig. 5a shows the O—O bond (1,090 cm^{-1}) formation during OER process, which represents the establishment of oxygen bridge between multi-metal sites [51]. The intensification of O—O signal with a higher overpotential is well aligned with prior studies asserting that O—O formation is the usual rate-determining step in OER [51,52]. The O—O bond formation in the observed wavelength corresponds specific to multi-metal sites, as opposed to a single metal site, confirming the mechanism belongs to the dual-metal-site mechanism (DMSM) discussed in a recent review by Zhang and Chai [53]. The multi-metal site mechanism could boost the kinetics of OER due to the direct O—O coupling and synergistic effect between the relevant metal atoms [54]. Additional FTIR spectra (Fig. S23) show characteristic bands at 3,590 and 1,560 cm^{-1} corresponding to the stretching and bending vibration of hydroxyl group on the surface [57]. These two peaks are intensified as the overpotential increases, indicating the adsorption of H_2O on the surface of the catalyst. The appearance of Ni—O—H bending vibration (617 cm^{-1}) is ascribed to the formation of hydroxide species on the surface of $Ni(OH)_2$, NiOOH, or both.

Moreover, from XPS results (Fig. 5b), the relative Ni^{3+}/Ni^{2+} ratio (Table S4) decreases from 0.74 at 1.23 V to 0.29 at 1.43 V and then increases to 0.69 at 1.63 V, while Co^{3+}/Co^{2+} (Table S5) exhibits the opposite trend, indicating a collaborative contribution of both metals to OER. In addition, the behavior of Ni^{3+}/Ni^{2+} ratio that synchronously mirrors the trend of oxygen vacancy concentration indicates that the formation of oxygen vacancies during OER occurs mostly around Ni, as opposed to Co. Overall, the trend of Ni and Co valence states and oxygen vacancy concentrations suggests that the active metal center (Ni and Co) directly couples with lattice oxygen to form O_2 molecular during OER process, in a good accordance with the lattice oxygen-mediated mechanism (LOM) as reported in the literature [55–58]. In the conventional OER mechanism where the reaction is believed to occur with a concerted proton-electron transfer on surface metal sites, the activity should not exhibit a pH-dependency [59,60]. The clear pH dependency of CoNi-BDC@LDH in OER activity (presented in Fig. S17) indicates that lattice oxygen species participate in the OER process.

3.5. Discussions

Based on the discussions above, the OER process in CoNi-BDC@LDH is proposed as follows. By incorporating an OH^- group on the surface, a deprotonation occurs from an existing hydroxyl group attached to Ni. Meanwhile, a lattice oxygen neighboring Ni is activated (i.e., the lattice oxygen moves to a neighboring low-valence-state Co site exposed to the surface) and forms an O—O bond along with the deprotonated oxygen. After this step, an oxygen vacancy is formed around Ni (step 1 in Fig. 6). Then, O_2 desorbs from the Ni—O—O—M (M: Ni or Co) bridge, and an additional incoming OH^- group is adsorbed onto a Ni (step 2). Then, the vacancy site next to Ni is occupied by another OH^- group introduced to the system (step 3). As the last step, the newly introduced OH is deprotonated to reach the initial state (step 4). In this proposed mechanism, Ni facilitates the desorption of O_2, forming an oxygen vacancy in its adjacent O sites for a subsequent OH^- adsorption, while Co serves as a strong Lewis acid to promote further oxidation of neighboring Ni [61].

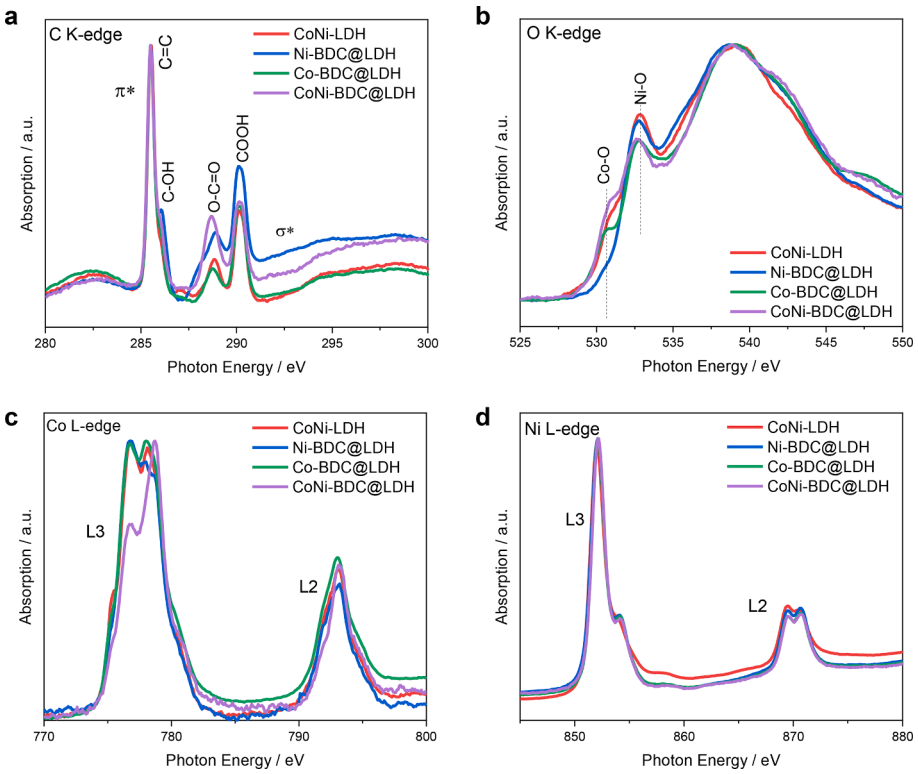

Fig. 4. Normalized XAS spectra of CoNi-LDH, Ni-BDC@LDH, Co-BDC@LDH, and CoNi-BDC@LDH. (a) C K-edge, (b) O K-edge, (c) Co L-edge and (d) Ni L-edge. For C K-edge spectra, the features at ~ 285.5 eV, 288.6 eV, and 290.0 eV are attributed to C=C, O-C=O, and C-OH bonding, respectively [41].

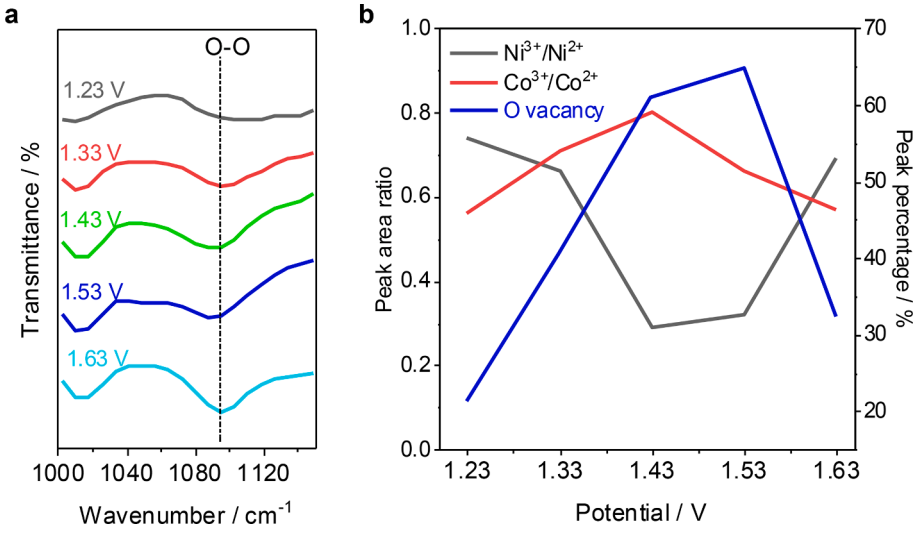

Fig. 5. (a) Zoomed-in ATR-FTIR spectra of CoNi-BDC@LDH under different potential showing O—O bond formation at 1090 cm^{-1}. (b) Trends of Co and Ni valency states and oxygen vacancy concentrations determined by XPS analysis (shown in Fig. S24) after exposing CoNi-BDC@LDH to different potentials.

Since the OER activity of all three BDC@LDH samples excels that of CoNi-LDH, it is reasonable to conjecture that the main OER activity of CoNi-BDC@LDH originate from Co-Ni sites residing at the interface of BDC and LDH, as opposed to within LDH itself.

The higher activity of CoNi-BDC@LDH, compared to Co-BDC@LDH and Ni-BDC@LDH, is ascribed to the richness of BDC and LDH interfaces where the aforementioned synergistic OER between neighboring Ni and Co sites occurs. At the bimetallic active sites, Co acts as a Lewis acid while Ni serves as the oxygen carrying species, by which its neighboring lattice oxygen is activated to form a Ni—O—O—M bridge for an efficient OER. It is also noted that the BDC-LDH interfaces are highly exposed to the surface in CoNi-BDC@LDH, unlike those in the other two samples as electron microscopy images indicated. For the same reason (i.e., the main active sites residing at the BDC-LDH interface), CoNi-BDC@LDH should exhibit a significantly higher performance than CoNi-LDH. Additionally, CoNi-BDC@LDH has a higher ECSA, and more of catalytically active CoOOH, $Ni(OH)_2$, and oxygen vacancies, all of which should further contribute to the activity.

4. Conclusion

In summary, we successfully fabricated a core–shell structure where

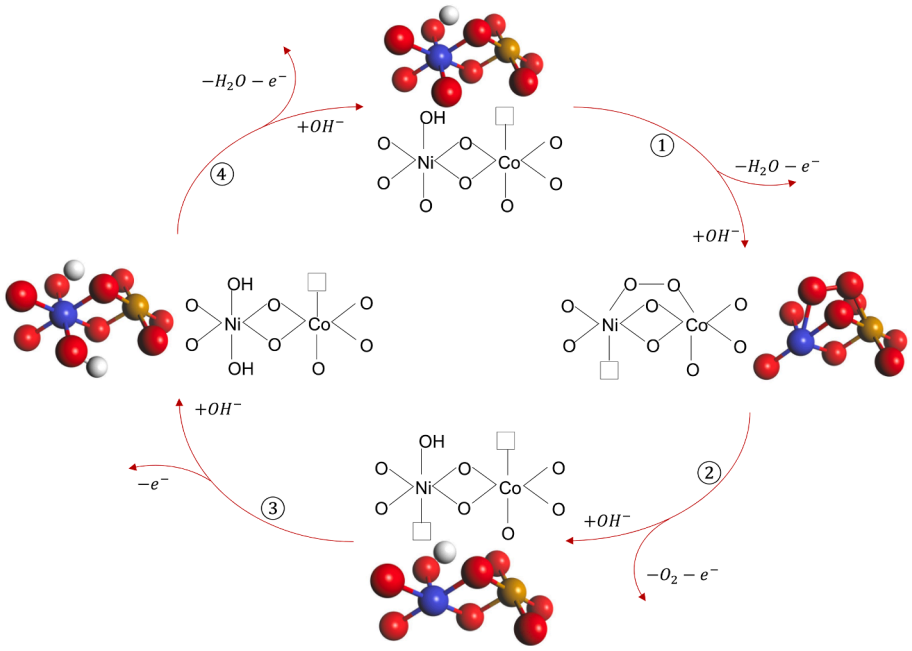

Fig. 6. A proposed OER dual-metal-site mechanism for CoNi-BDC@LDH. The bimetallic active site is conjectured to reside mainly at the interface between BDC and LDH.

CoNi-LDH nanoplates are grown on the surface of cuboidal MOFs via a facile one-pot synthesis strategy. A unique 3D polyhedron microstructure with a coverage of numerous nanoplates is constructed by using urea as the surface coordination buffer between LDHs and MOFs and regulating the order of precursor introduction during synthesis. CoNi-BDC@LDH demonstrates an excellent catalytic performance toward OER, with the overpotential of 282 mV at 100 mA cm^{-2} and Tafel slope of 105 mV dec^{-1} in 1 M KOH. It also exhibits an excellent chronoamperometric stability for over 20 h and cyclic stability over 2,000 CV cycles. The MOF structure (core) in the core–shell structure is expected to act as the scaffold onto which LDH nanosheets (shell) grow, thereby suppressing the aggregation of the LDH sheets and providing a higher catalytically active area. From a series of *quasi-operando* and *ex situ* studies by Raman, ATR-FTIR, XPS and XAS, we further revealed the intrinsic active sites in the best-performing catalyst. The desorption of O_2 from Ni—O—O—M bridge, which is conjectured to form mainly at the interface between LDH and BDC structures, is prompted on the multi-metal-site on the LDH surface, and upon the desorption of O_2, a subsequent OH^- is adsorbed in the O site next to the Ni. Along with the synergistic bimetallic effect, the high electrochemical surface area, and the formation of CoOOH and γ-NiOOH concertedly contributes to the enhanced OER performance. This work contributes to a general strategy for a rational design of multi-metallic hierarchical core–shell structures, and *quasi-operando* studies for revealing dynamic active sites during electrochemical processes.

Declaration of Competing Interest

The authors declare that they have no known competing financial interests or personal relationships that could have appeared to influence the work reported in this paper.

Data availability

Data will be made available on request.

Acknowledgements

This work was supported by the NASA MIRO program (Grant No. NNX15AQ01A). The X-ray absorption testing was performed by using the resources at the Advanced Light Source, a U.S. DOE Office of Science User Facility under contract no. DE-AC02-05CH11231.

Appendix A. Supplementary data

Supplementary data to this article can be found online at https://doi.org/10.1016/j.cej.2022.140403.

References

[1] S.Y. Tee, K.Y. Win, W.S. Teo, L.-D. Koh, S. Liu, C.P. Teng, M.-Y. Han, Recent Progress in Energy-Driven Water Splitting, Adv. Sci. 4 (2017) 1600337.
[2] D. Yang, L. Zhang, X. Yan, X. Yao, Recent Progress in Oxygen Electrocatalysts for Zinc-Air Batteries, Small Methods. 1 (2017) 1700209.
[3] L. Li, J. He, Y. Wang, X. Lv, X. Gu, P. Dai, D. Liu, X. Zhao, Metal–organic frameworks: a promising platform for constructing non-noble electrocatalysts for the oxygen-reduction reaction, J. Mater. Chem. A. 7 (2019) 1964–1988.
[4] H. Li, H.-S. Kang, S. Grewal, A.J. Nelson, S.A. Song, M.H. Lee, How an angstrom-thick oxide overcoat enhances durability and activity of nanoparticle-decorated cathodes in solid oxide fuel cells, J. Mater. Chem. A. 8 (31) (2020) 15927–15935.
[5] M. Liu, L. Wang, K. Zhao, S. Shi, Q. Shao, L. Zhang, X. Sun, Y. Zhao, J. Zhang, Atomically dispersed metal catalysts for the oxygen reduction reaction: synthesis, characterization, reaction mechanisms and electrochemical energy applications, Energy Environ. Sci. 12 (2019) 2890–2923.
[6] R. Frydendal, E.A. Paoli, B.P. Knudsen, B. Wickman, P. Malacrida, I.E.L. Stephens, I. Chorkendorff, Benchmarking the Stability of Oxygen Evolution Reaction Catalysts: The Importance of Monitoring Mass Losses, ChemElectroChem. 1 (2014) 2075–2081.
[7] Y. Lee, J. Suntivich, K.J. May, E.E. Perry, Y. Shao-Horn, Synthesis and activities of rutile IrO 2 and RuO 2 nanoparticles for oxygen evolution in acid and alkaline solutions, J. Phys. Chem. Lett. 3 (3) (2012) 399–404.
[8] T. Reier, M. Oezaslan, P. Strasser, Electrocatalytic oxygen evolution reaction (OER) on Ru Ir, and pt catalysts: A comparative study of nanoparticles and bulk materials, ACS Catal. 2 (2012) 1765–1772.
[9] M. Gao, W. Sheng, Z. Zhuang, Q. Fang, S. Gu, J. Jiang, Y. Yan, Efficient water oxidation using nanostructured α-nickel-hydroxide as an electrocatalyst, J. Am. Chem. Soc. 136 (19) (2014) 7077–7084.
[10] L. Lv, Z. Yang, K. Chen, C. Wang, Y. Xiong, 2D Layered Double Hydroxides for Oxygen Evolution Reaction: From Fundamental Design to Application, Adv. Energy Mater. 9 (2019) 1803358.
[11] J. Zhang, L. Yu, Y. Chen, F. Lu, S. Gao, X. Wen, D. Lou, J.T. Zhang, L. Yu, X.F. Lu, X. W. Lou, Y. Chen, S.Y. Gao, Designed Formation of Double-Shelled Ni–Fe Layered-Double-Hydroxide Nanocages for Efficient Oxygen Evolution Reaction, Adv. Mater. 32 (2020) 1906432.

[12] B.W. Xue, C.H. Zhang, Y.Z. Wang, W.W. Xie, N.-W. Li, L.e. Yu, Recent progress of Ni–Fe layered double hydroxide and beyond towards electrochemical water splitting, Nanoscale Adv. 2 (12) (2020) 5555–5566.
[13] P. Zhai, M. Xia, Y. Wu, G. Zhang, J. Gao, B. Zhang, S. Cao, Y. Zhang, Z. Li, Z. Fan, C. Wang, X. Zhang, J.T. Miller, L. Sun, J. Hou, Engineering single-atomic ruthenium catalytic sites on defective nickel-iron layered double hydroxide for overall water splitting, Nat. Commun. 12 (2021) 4587.
[14] K.B. Ibrahim, M.-C. Tsai, S.A. Chala, M.K. Berihun, A.W. Kahsay, T.A. Berhe, W.-N. Su, B.-J. Hwang, A review of transition metal-based bifunctional oxygen electrocatalysts, J. Chinese Chem. Soc. 66 (8) (2019) 829–865.
[15] D.S. Hall, D.J. Lockwood, C. Bock, B.R. MacDougall, Nickel hydroxides and related materials: a review of their structures, synthesis and properties, Proc. R. Soc. A Math. Phys. Eng. Sci. 471 (2015) 20140792.
[16] Z. Cai, X. Bu, P. Wang, J.C. Ho, J. Yang, X. Wang, Recent advances in layered double hydroxide electrocatalysts for the oxygen evolution reaction, J. Mater. Chem. A. 7 (10) (2019) 5069–5089.
[17] J. Huo, Y. Wang, L. Yan, Y. Xue, S. Li, M. Hu, Y. Jiang, Q.-G. Zhai, In situ semi-transformation from heterometallic MOFs to Fe–Ni LDH/MOF hierarchical architectures for boosted oxygen evolution reaction, Nanoscale 12 (27) (2020) 14514–14523.
[18] M. Shao, R. Zhang, Z. Li, M. Wei, D.G. Evans, X. Duan, Layered double hydroxides toward electrochemical energy storage and conversion: design, synthesis and applications, Chem. Commun. 51 (2015) 15880–15893.
[19] H.S. Jadhav, A. Roy, B.Z. Desalegan, J.G. Seo, An advanced and highly efficient Ce assisted NiFe-LDH electrocatalyst for overall water splitting, Sustain, Energy Fuels. 4 (1) (2020) 312–323.
[20] L.u. Ni, J. Zhou, N. Chen, X. Li, S. Xu, L. Zhang, C. Lu, J. Chen, L. Xu, W. Hou, In situ direct growth of flower-like hierarchical architecture of CoNi-layered double hydroxide on Ni foam as an efficient self-supported oxygen evolution electrocatalyst, Int. J. Hydrogen Energy. 45 (43) (2020) 22788–22796.
[21] Y. Luo, Y. Wu, D. Wu, C. Huang, D. Xiao, H. Chen, S. Zheng, P.K. Chu, NiFe-Layered Double Hydroxide Synchronously Activated by Heterojunctions and Vacancies for the Oxygen Evolution Reaction, ACS Appl. Mater. Interfaces. 12 (38) (2020) 42850–42858.
[22] C. Ye, L. Zhang, L. Yue, B. Deng, Y. Cao, Q. Liu, Y. Luo, S. Lu, B. Zheng, X. Sun, A NiCo LDH nanosheet array on graphite felt: an efficient 3D electrocatalyst for the oxygen evolution reaction in alkaline media, Inorg. Chem. Front. 8 (2021) 3162–3166.
[23] P. Zhai, Y. Zhang, Y. Wu, J. Gao, B. Zhang, S. Cao, Y. Zhang, Z. Li, L. Sun, J. Hou, Engineering active sites on hierarchical transition bimetal oxides/sulfides heterostructure array enabling robust overall water splitting, Nat. Commun. 11 (2020) 5462.
[24] M. Xiao, C. Zhang, P. Wang, W. Zeng, J. Zhu, Y. Li, W. Peng, Q. Liu, H. Xu, Y. Zhao, H. Li, L. Chen, J. Yu, S. Mu, Polymetallic phosphides evolved from MOF and LDH dual-precursors for robust oxygen evolution reaction in alkaline and seawater media, Mater. Today Phys. 24 (2022), 100684.
[25] H. Xu, C. Shan, X. Wu, M. Sun, B. Huang, Y.u. Tang, C.-H. Yan, Fabrication of layered double hydroxide microcapsules mediated by cerium doping in metal–organic frameworks for boosting water splitting, Energy Environ. Sci. 13 (9) (2020) 2949–2956.
[26] W. Wang, Y. Lu, M. Zhao, R. Luo, Y.a. Yang, T. Peng, H. Yan, X. Liu, Y. Luo, Controllable Tuning of Cobalt Nickel-Layered Double Hydroxide Arrays as Multifunctional Electrodes for Flexible Supercapattery Device and Oxygen Evolution Reaction, ACS Nano 13 (10) (2019) 12206–12218.
[27] W. He, X. Li, S. An, T. Li, Y. Zhang, J. Cui, 3D β-Ni(OH)2 nanowires/RGO composite prepared by phase transformation method for superior electrochemical performance, Sci. Rep. 9 (2019) 10838.
[28] Y. Si, C. Guo, C. Xie, Z. Xiong, An Ultrasonication-Assisted Cobalt Hydroxide Composite with Enhanced Electrocatalytic Activity toward Oxygen Evolution Reaction, Materials (Basel) 11 (2018) 1912.
[29] C.A. Téllez S, E. Hollauer, M.A. Mondragon, V.M. Castaño, Fourier transform infrared and Raman spectra, vibrational assignment and ab initio calculations of terephthalic acid and related compounds, Spectrochim. Acta Part A Mol. Biomol. Spectrosc. 57 (5) (2001) 993–1007.
[30] F. Millange, C. Serre, G. Férey, Synthesis, structure determination and properties of MIL-53as and MIL-53ht: the first Criii hybrid inorganic–organic microporous solids: Criii(OH)·{O2C–C6H4–CO2}·{HO2C–C6H4–CO2H}, Chem. Commun. 822–823 (2002).
[31] D. Salionov, O.O. Semivrazhskaya, N.P.M. Casati, M. Ranocchiari, S. Bjelić, R. Verel, J.A. van Bokhoven, V.L. Sushkevich, Unraveling the molecular mechanism of MIL-53(Al) crystallization, Nat. Commun. 13 (2022) 3762.
[32] Z. Ni, Y. Wang, T. Yu, Z. Shen, Raman spectroscopy and imaging of graphene, Nano Res. 1 (4) (2008) 273–291.
[33] X. Meng, M. Feng, H. Zhang, Z. Ma, C. Zhang, Solvothermal synthesis of cobalt/nickel layered double hydroxides for energy storage devices, J. Alloys Compd. 695 (2017) 3522–3529.
[34] J.-H. Zhong, A.-L. Wang, G.-R. Li, J.-W. Wang, Y.-N. Ou, Y.-X. Tong, Co3O4/Ni(OH)2 composite mesoporous nanosheet networks as a promising electrode for supercapacitor applications, J. Mater. Chem. 22 (2012) 5656.
[35] J. Jiang, F. Sun, S. Zhou, W. Hu, H. Zhang, J. Dong, Z. Jiang, J. Zhao, J. Li, W. Yan, M. Wang, Atomic-level insight into super-efficient electrocatalytic oxygen evolution on iron and vanadium co-doped nickel (oxy)hydroxide, Nat. Commun. 9 (2018) 2885.
[36] B. Wang, J. Jin, B. Ding, X. Han, A. Han, J. Liu, General Approach to Metal-Organic Framework Nanosheets With Controllable Thickness by Using Metal Hydroxides as Precursors, Front. Mater. 7 (2020) 37.
[37] Z. Gao, J. Liu, X. Chen, X. Zheng, J. Mao, H. Liu, T. Ma, L. Li, W. Wang, X. Du, Engineering NiO/NiFe LDH Intersection to Bypass Scaling Relationship for Oxygen Evolution Reaction via Dynamic Tridimensional Adsorption of Intermediates, Adv. Mater. 31 (2019) 1804769.
[38] D. Ping, X. Feng, J. Zhang, J. Geng, X. Dong, Directed Growth of a Bimetallic MOF Membrane and the Derived NiCo Alloy@C/Ni x Co 1–x O/Ni Foam Composite as an Efficient Electrocatalyst for the Oxygen Evolution Reaction, ChemElectroChem 4 (12) (2017) 3037–3041.
[39] Z. Dai, X. Du, X. Zhang, Controlled synthesis of NiCo2O4@Ni-MOF on Ni foam as efficient electrocatalyst for urea oxidation reaction and oxygen evolution reaction, Int. J. Hydrogen Energy. 47 (39) (2022) 17252–17262.
[40] H.Y. Wang, Y.Y. Hsu, R. Chen, T.S. Chan, H.M. Chen, B. Liu, Ni3+-Induced Formation of Active NiOOH on the Spinel Ni–Co Oxide Surface for Efficient Oxygen Evolution Reaction, Adv. Energy Mater. 5 (2015) 1500091.
[41] Y. Liang, H. Wang, J. Zhou, Y. Li, J. Wang, T. Regier, H. Dai, Covalent Hybrid of Spinel Manganese-Cobalt Oxide and Graphene as Advanced Oxygen Reduction Electrocatalysts, J. Am. Chem. Soc. 134 (7) (2012) 3517–3523.
[42] L. Zhang, X. Li, A. Augustsson, C.M. Lee, J.E. Rubensson, J. Nordgren, P.N. Ross, J. H. Guo, Revealing the electronic structure of LiC6 by soft X-ray spectroscopy, Appl. Phys. Lett. 110 (2017), 104106.
[43] Y. Zhang, O. Kizilkaya, H.K. Bilan, R. Kurtz, E.J. Podlaha, Activity and Regeneration of Electrodeposited Fe–Ni–Co-Based Electrocatalysts for the Alkaline Oxygen Evolution Reaction, ACS Appl. Energy Mater. 3 (8) (2020) 7239–7245.
[44] D. Drevon, M. Görlin, P. Chernev, L. Xi, H. Dau, K.M. Lange, Uncovering The Role of Oxygen in Ni-Fe(OxHy) Electrocatalysts using In situ Soft X-ray Absorption Spectroscopy during the Oxygen Evolution Reaction, Sci. Rep. 9 (2019) 1532.
[45] J. Yang, C. Yu, C. Hu, M. Wang, S. Li, H. Huang, K. Bustillo, X. Han, C. Zhao, W. Guo, Z. Zeng, H. Zheng, J. Qiu, Surface-Confined Fabrication of Ultrathin Nickel Cobalt-Layered Double Hydroxide Nanosheets for High-Performance Supercapacitors, Adv. Funct. Mater. 28 (2018) 1803272.
[46] M.L. Baker, M.W. Mara, J.J. Yan, K.O. Hodgson, B. Hedman, E.I. Solomon, K- and L-edge X-ray absorption spectroscopy (XAS) and resonant inelastic X-ray scattering (RIXS) determination of differential orbital covalency (DOC) of transition metal sites, Coord. Chem. Rev. 345 (2017) 182–208.
[47] X.X. Wang, D.A. Cullen, Y.-T. Pan, S. Hwang, M. Wang, Z. Feng, J. Wang, M. H. Engelhard, H. Zhang, Y. He, Y. Shao, D. Su, K.L. More, J.S. Spendelow, G. Wu, Nitrogen-Coordinated Single Cobalt Atom Catalysts for Oxygen Reduction in Proton Exchange Membrane Fuel Cells, Adv. Mater. 30 (2018) 1706758.
[48] S. Zhao, C. Tan, C.-T. He, P. An, F. Xie, S. Jiang, Y. Zhu, K.-H. Wu, B. Zhang, H. Li, J. Zhang, Y. Chen, S. Liu, J. Dong, Z. Tang, Structural transformation of highly active metal–organic framework electrocatalysts during the oxygen evolution reaction, Nat. Energy. 5 (11) (2020) 881–890.
[49] Z. Qiu, C.-W. Tai, G.A. Niklasson, T. Edvinsson, Direct observation of active catalyst surface phases and the effect of dynamic self-optimization in NiFe-layered double hydroxides for alkaline water splitting, Energy Environ. Sci. 12 (2) (2019) 572–581.
[50] Y. Wu, Y. Zhao, P. Zhai, C. Wang, J. Gao, L. Sun, J. Hou, Triggering Lattice Oxygen Activation of Single-Atomic Mo Sites Anchored on Ni–Fe Oxyhydroxides Nanoarrays for Electrochemical Water Oxidation, Adv. Mater. 34 (2022) 2202523.
[51] B. Wang, K. Zhao, Z. Yu, C. Sun, Z. Wang, N. Feng, L. Mai, Y. Wang, Y. Xia, In situ structural evolution of the multi-site alloy electrocatalyst to manipulate the intermediate for enhanced water oxidation reaction, Energy Environ. Sci. 13 (7) (2020) 2200–2208.
[52] Y. Li, X. Du, J. Huang, C. Wu, Y. Sun, G. Zou, C. Yang, J. Xiong, Recent Progress on Surface Reconstruction of Earth-Abundant Electrocatalysts for Water Oxidation, Small. 15 (2019) 1901980.
[53] N. Zhang, Y. Chai, Lattice oxygen redox chemistry in solid-state electrocatalysts for water oxidation, Energy Environ. Sci. 14 (9) (2021) 4647–4671.
[54] T. Wu, S. Sun, J. Song, S. Xi, Y. Du, B. Chen, W.A. Sasangka, H. Liao, C.L. Gan, G. G. Scherer, L. Zeng, H. Wang, H. Li, A. Grimaud, Z.J. Xu, Iron-facilitated dynamic active-site generation on spinel CoAl2O4 with self-termination of surface reconstruction for water oxidation, Nat. Catal. 29 (2) (2019 2019,) 763–772.
[55] R.G. Gast, E.R. Landa, G.W. Meyer, The Interaction of Water with Goethite (α-FeOOH) and Amorphous Hydrated Ferric Oxide Surfaces, Clays Clay Miner. 221 (22) (1974 1974,) 31–39.
[56] M. Kim, J. Park, M. Kang, J.Y. Kim, S.W. Lee, Toward Efficient Electrocatalytic Oxygen Evolution: Emerging Opportunities with Metallic Pyrochlore Oxides for Electrocatalysts and Conductive Supports, ACS Cent. Sci. 6 (2020) 880–891.
[57] Y.-C. Zhang, C. Han, J. Gao, L. Pan, J. Wu, X.-D. Zhu, J.-J. Zou, NiCo-Based Electrocatalysts for the Alkaline Oxygen Evolution Reaction: A Review, ACS Catal. 11 (20) (2021) 12485–12509.
[58] Z.-F. Huang, J. Song, S. Dou, X. Li, J. Wang, X. Wang, Strategies to Break the Scaling Relation toward Enhanced Oxygen Electrocatalysis, Matter. 1 (6) (2019) 1494–1518.
[59] A. Grimaud, O. Diaz-Morales, B. Han, W.T. Hong, Y.-L. Lee, L. Giordano, K. A. Stoerzinger, M.T.M. Koper, Y. Shao-Horn, Activating lattice oxygen redox reactions in metal oxides to catalyse oxygen evolution, Nat. Chem. 9 (5) (2017) 457–465.
[60] X. Xu, Y. Pan, Y. Zhong, C. Shi, D. Guan, L. Ge, Z. Hu, Y. Chin, H. Lin, C. Chen, H. Wang, S.P. Jiang, Z. Shao, New Undisputed Evidence and Strategy for Enhanced Lattice-Oxygen Participation of Perovskite Electrocatalyst through Cation Deficiency Manipulation, Adv. Sci. 9 (2022) 2200530.
[61] N. Li, D.K. Bediako, R.G. Hadt, D. Hayes, T.J. Kempa, F. von Cube, D.C. Bell, L. X. Chen, D.G. Nocera, Influence of iron doping on tetravalent nickel content in catalytic oxygen evolving films, Proc. Natl. Acad. Sci. U. S. A. 114 (7) (2017) 1486–1491.